communications materials

A Nature Portfolio journal

Article

https://doi.org/10.1038/s43246-026-01270-2

Enhanced charge-density-wave order and suppressed superconductivity in intercalated bulk $NbSe_2$

Huanhuan Shi[1,8] ✉, Qili Li[2], Antoine M. T. Baron[1,3], Marie-Aude Méasson[3], Sangjun Kang[4,5,6], Dirk Fuchs[1], Fabian Henssler[1], Alexander Haas[2], Di Wang[4,6], Paolo Battistoni[1], Konstantin Semeniuk[1], Elena Hassinger[1,7], Nour Maraytta[1], Michael Merz[1,6], Amir-Abbas Haghighirad[1], Wulf Wulfhekel[1,2], Christian Kübel[4,5,6] & Matthieu Le Tacon[1] ✉

The electronic ground states of transition-metal dichalcogenides are strongly shaped by reduced dimensionality, yet the properties of atomically thin layers remain difficult to probe due to their small size and environmental sensitivity. Here we demonstrate that controlled electrochemical intercalation of organic cations provides a robust bulk platform for accessing monolayer-like physics in $NbSe_2$. Intercalation of tetrapropylammonium and tetrabutylammonium expands the interlayer spacing by nearly a factor of two, electronically decoupling the $NbSe_2$ layers while simultaneously introducing well-defined charge doping. Using a combination of Raman spectroscopy, scanning tunneling microscopy, X-ray diffraction, and photoemission, we uncover a pronounced enhancement of the charge-density-wave transition temperature to ~ 130 K together with a strong suppression of superconductivity, reproducing the phase diagram observed in exfoliated monolayers. The enhanced charge-density-wave order and reduced T_c arise from the combined effects of dimensionality reduction and electron injection, and are accompanied by distinct dip-hump anomalies in the tunneling spectra suggestive of collective mode excitations. Our results establish molecular intercalation as a powerful and scalable route for engineering competing orders in layered quantum materials.

The reduced dimensionality of monolayer transition-metal dichalcogenides (TMDs) gives rise to distinctive physical properties absent in bulk crystals, spurring intense research activity in the field of low-dimensional materials[1,2]. At the monolayer limit, direct band gaps in the visible range, strong spin–orbit coupling, and pronounced excitonic effects emerge, enabling phenomena and applications that are inaccessible in the bulk compound.

Bulk TMD 2H-$NbSe_2$ has a hexagonal structure with space group $P6_3/mmc$ and hosts both a charge-density-wave (CDW) order and superconductivity, emerging below $T_{CDW} = 33$ K and $T_c = 7.2$ K, respectively. The interplay between these two orders has been extensively investigated[3–6]. Beyond its rich phase diagram, 2H-$NbSe_2$ serves as a model system to study CDW formation in dimensions $d > 1$, where the canonical Peierls picture of Fermi-surface-nesting-driven CDWs breaks down. Instead, the nearly commensurate instability at q_{CDW} = (0.329, 0, 0) [7], responsible for the characteristic ~3 × 3 superstructure, was shown to originate from anisotropic electron–phonon coupling[8,9]. The superconductivity in this material is also believed to be conventional in nature[10], arising from the same electron–phonon interaction[3], making $NbSe_2$ a valuable platform for exploring the microscopic coupling between CDW and superconducting states.

A particularly appealing aspect of $NbSe_2$ is its tunability. External pressure[3,11–13], strain[14], structural modifications such as misfit phases[15–17], and, most prominently, reduction in dimensionality to the monolayer limit[18,19], all strongly reshape the balance between CDW and superconductivity, offering important insights into their microscopic origin.

[1]Institute for Quantum Materials and Technologies, Karlsruhe Institute of Technology, Karlsruhe, Germany. [2]Physikalisches Institut, Karlsruhe Institute of Technology, Karlsruhe, Germany. [3]Institut Néel CNRS/UGA UPR2940, Grenoble, France. [4]Institute of Nanotechnology, Karlsruhe Institute of Technology, Karlsruhe, Germany. [5]In-situ Electron Microscopy, Department of Materials and Earth Sciences, Technische Universität Darmstadt, Darmstadt, Germany. [6]Karlsruhe Nano Micro Facility (KNMFi), Karlsruhe Institute of Technology, Karlsruhe, Germany. [7]Max Planck Institute for Chemical Physics of Solids, Dresden, Germany. [8]Present address: College of Materials Science and Engineering, Hunan University, Changsha, China. ✉e-mail: hh.shi@foxmail.com; matthieu.letacon@kit.edu

The monolayer $NbSe_2$ prepared by mechanical exfoliation provides an ideal platform for examining these competing orders in the two-dimensional limit[20,21]. Owing to its non-centrosymmetric structure and strong spin–orbit coupling, monolayer $NbSe_2$ hosts Ising superconductivity, a phenomenon absent in the bulk[22]. In this regime, T_c is strongly reduced to 0.9–3.7 K, while T_{CDW} increases rapidly, reaching 145 K[19]. In particular, this enhancement occurs without a change in the CDW wave vector[18,23]. The opposing evolution of T_c and T_{CDW} reinforces the competitive relationship between CDW formation and superconductivity. Nevertheless, the microscopic mechanisms driving CDW order and superconductivity[24,25], and the origins of their interplay[3,9,13,26], remain the subject of active debate.

Despite their utility, exfoliated monolayers suffer from intrinsic limitations, including micron-scale lateral dimensions, time-consuming preparation, and air sensitivity, which restrict the range of experimental probes that can be reliably applied. To circumvent these challenges, chemical intercalation has emerged as an effective strategy to suppress interlayer coupling in bulk crystals and induce monolayer-like behavior without the need for exfoliation[27]. Beyond decoupling layers, intercalated ions can donate charge carriers, providing simultaneous control over dimensionality and electron density[28,29].

This approach has recently been brought to bear on $NbSe_2$. For example, Zhang et al. demonstrated that ionic-liquid intercalation results in a suppressed $T_{CDW} \approx 68$ K and enhanced $T_c \approx 6.9$ K compared to monolayer samples[30]. Similarly, tetraheptylammonium-intercalated $NbSe_2$ exhibits $T_{CDW} = 65$ K and $T_c = 7.1$ K[31]. These observations further support the competitive nature of CDW and superconductivity. However, intercalated $NbSe_2$ has not yet displayed the concurrent enhancement of T_{CDW} and suppression of the superconducting transition temperature that is characteristic of the true monolayer limit.

In this work, we synthesize large-area (~1 mm) intercalated $NbSe_2$ crystals using variable-size organic cations (tetrapropylammonium (TPA^+) and tetrabutylammonium (TBA^+)) to systematically tune the interlayer spacing and carrier concentration. X-ray diffraction (XRD) and high-angle annular dark-field scanning transmission electron microscopy (HAADF-STEM) confirm that intercalation expands the interlayer spacing from 0.62 nm in the bulk to 1.22 nm in $(TPA)_yNbSe_2$ and 1.52 nm in $(TBA)_xNbSe_2$, effectively decoupling adjacent layers. Raman spectroscopy reveals a pronounced enhancement of T_{CDW} to 70 K in $(TPA)_yNbSe_2$ and a record-high 130 K in $(TBA)_xNbSe_2$, while scanning tunneling microscopy (STM) shows a strong suppression of the local superconducting gap Δ_{SC}. Low-temperature transport and magnetization measurements further show that superconductivity persists in the intercalated crystals, although the comparison with STM indicates a spatially inhomogeneous superconducting response. Notably, $(TBA)_xNbSe_2$ exhibits charge-order behavior closely resembling that of exfoliated monolayers. These results support the intrinsic competition between CDW formation and superconductivity in $NbSe_2$ and establish molecular intercalation as a powerful route to access monolayer-like physics in bulk crystals.

Results

The structural effects of molecular intercalation (detailed in the "Methods" section) were investigated using a combination of Raman spectroscopy, XRD, and TEM. Reference Raman spectra obtained from pristine 2H-$NbSe_2$ single crystals are presented in Supplementary Fig. 9 and exhibit all characteristic phonon modes previously reported at room temperature for this material. These include the A_{1g} mode (out-of-plane vibrations) at 234 cm^{-1}, the E^1_{2g} mode (in-plane vibrations) at 250 cm^{-1}, the soft mode (associated with a second-order scattering process) at 181 cm^{-1}, and the E^2_{2g} shear mode at 30 cm^{-1}. These features are well established in the literature for bulk $NbSe_2$[32].

A direct signature of intercalation is shown in Fig. 2-a, where a systematic redshift of the A_{1g} mode is observed in the intercalated compounds (see full spectra in Supplementary Fig. 10). Notably, the phonon lineshape remains similar to that of the pristine sample, indicating good structural integrity after intercalation. Relative to pristine 2H-$NbSe_2$, the A_{1g} mode softens by 4.2 cm^{-1} in $(TPA)_yNbSe_2$ and by 5 cm^{-1} in $(TBA)_xNbSe_2$, consistent with lattice expansion along the *c*-axis. The additional 0.8 cm^{-1} redshift observed in $(TBA)_xNbSe_2$ relative to $(TPA)_yNbSe_2$ suggests that the larger TBA^+ cation is more effective in weakening interlayer coupling in $NbSe_2$.

More importantly, a substantial hardening of 9 cm^{-1} in the E^1_{2g} mode, as well as a complete suppression of the shear mode, is observed in the intercalated samples. These behaviors closely mirror those of the monolayer $NbSe_2$[19,33]. Taken together, these results strongly suggest that the intercalated compounds effectively replicate the physical characteristics of the monolayer $NbSe_2$.

Building on the Raman evidence for weakened interlayer coupling, we turn to XRD and cross-sectional TEM to quantitatively determine the interlayer separation and confirm the configuration adopted by the intercalated species. Indeed, tetraalkylammonium (TAA^+) ions can exist in two primary configurations: a flattened form and a tetrahedral form (see Supplementary Fig. 3)[34]. Figure 2b compares the XRD patterns of the pristine and intercalated samples. The pristine crystal $NbSe_2$ exhibits sharp diffraction peaks (00ℓ), corresponding to an interlayer spacing of 0.62 nm, in agreement with previous reports[31]. Upon intercalation, the (00ℓ) reflections of the pristine $NbSe_2$ disappear entirely, and a new set of (00ℓ) peaks without obvious peak splitting appears at lower 2θ angles in the intercalated $NbSe_2$. This indicates that, within the bulk sensitivity of XRD, the intercalated phase is dominant and that no sizeable fraction of non-intercalated $NbSe_2$ remains. According to XRD results, the interlayer distances of $(TPA)_yNbSe_2$ and $(TBA)_xNbSe_2$ are 1.22 nm and 1.52 nm, respectively. Compared to pristine $NbSe_2$, the interlayer distances expand by ~0.6 nm for $(TPA)_yNbSe_2$ and 0.9 nm for $(TBA)_xNbSe_2$. Notably, the expansion of $(TPA)_yNbSe_2$ is larger than a flattened form (0.4 nm) but smaller than a tetrahedral form (0.78 nm) of TPA^+, suggesting the presence of a distorted tetrahedral configuration of TPA^+. In contrast, the expanded interlayer spacing observed for $(TBA)_xNbSe_2$ is in good agreement with the tetrahedral TBA^+ cation, providing strong evidence that intercalation occurs by insertion of a single TBA^+ ion into its tetrahedral conformation (Fig. 1). This conformation is further corroborated by cross-sectional HAADF-STEM imaging (Fig. 2c and Supplementary Fig. 6), which reveals a continuous and regularly spaced lamellar structure over the imaged region, with an interlayer spacing consistent with the value extracted from XRD. These observations support a largely homogeneous expansion of the van der Waals gaps.

Having determined both the conformation of the intercalated TAA^+ cations and the associated lattice expansion, we now turn to the effect of intercalation on the CDW properties of $NbSe_2$. Figures 3 and S10 present temperature-dependent Raman spectra of pristine and intercalated $NbSe_2$ measured between 10 and 290 K. The *ab* polarization configuration was

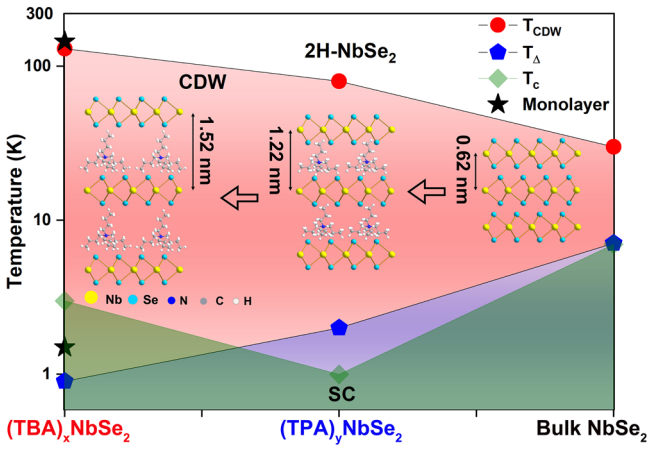

Fig. 1 | Intercalant–temperature phase diagram of 2H-$NbSe_2$. T_{CDW} is determined from Raman spectroscopy. Superconducting transition temperatures from transport/magnetization (T_c) are shown separately from the local superconducting gap scale measured by STM ($T_\Delta = 2\Delta_{SC}/(3.52k_B)$). Monolayer values are taken from ref. 19.

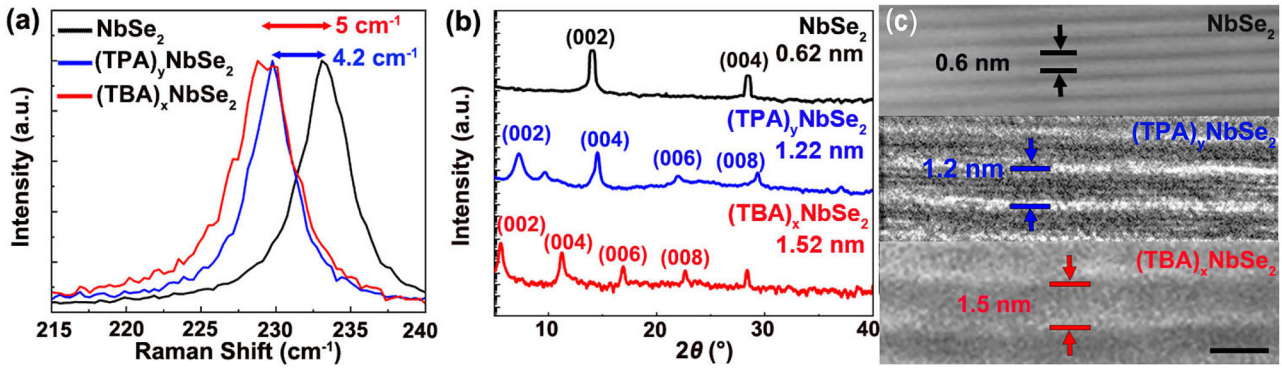

Fig. 2 | Structural characterization of intercalated $NbSe_2$. **a** A_{1g} mode of $NbSe_2$, $(TPA)_yNbSe_2$ and $(TBA)_xNbSe_2$. **b** XRD patterns of $NbSe_2$, $(TPA)_yNbSe_2$ and $(TBA)_xNbSe_2$. **c** Cross-sectional HAADF-STEM images of pristine $NbSe_2$ (top), intercalated $(TPA)_yNbSe_2$ and $(TBA)_xNbSe_2$ (bottom). Scale bars, 1 nm.

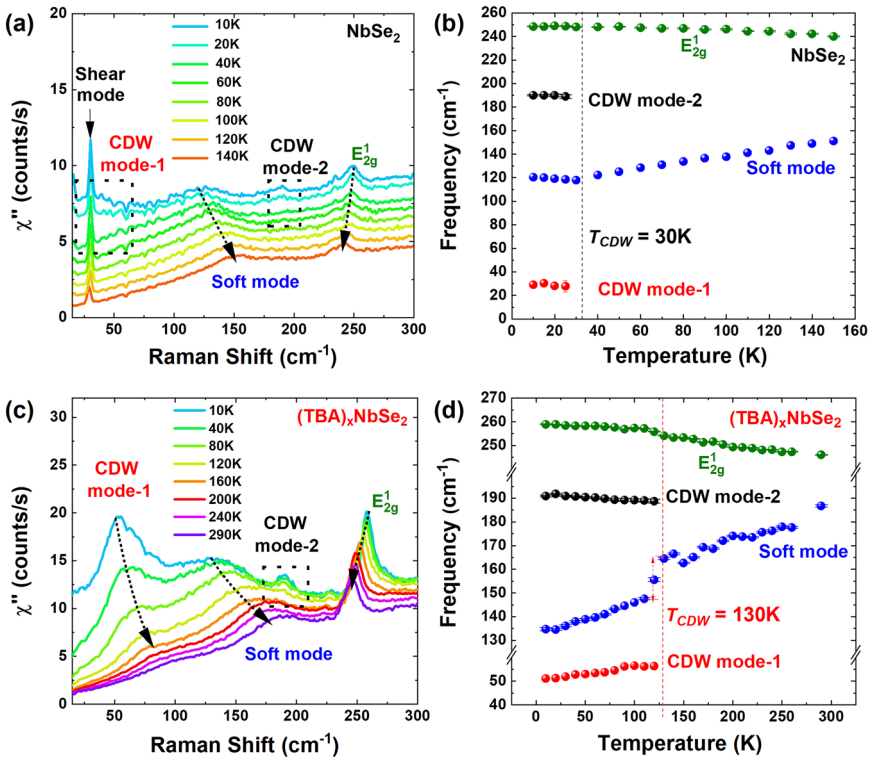

Fig. 3 | Raman evidence for enhanced charge-density-wave order in intercalated $NbSe_2$. **a**, **c** Temperature-dependent Raman spectra of pristine $NbSe_2$ (**a**) and intercalated $(TBA)_xNbSe_2$ (**c**) in the ab polarization configuration. **b**, **d** Temperature dependence of the phonon frequencies in pristine $NbSe_2$ (**b**) and intercalated $(TBA)_xNbSe_2$ (**d**).

used to minimize the background of elastic scattering, and all spectra were corrected for by the temperature-dependent Bose factor[35].

In pristine $NbSe_2$, the soft mode redshifts upon cooling and saturates at 117.8 cm^{-1} below the CDW transition temperature T_{CDW} = 33 K (Fig. 3a). At lower temperatures, two additional Raman modes emerge at 28 cm^{-1} (amplitude mode) and 189 cm^{-1}, signaling the onset of CDW order, consistent with previous reports[36–38]. Strikingly, these CDW-associated modes appear at significantly higher temperatures in intercalated $NbSe_2$ (Fig. 3c and Supplementary Fig. 12). The high-frequency mode remains near 189 cm^{-1}, while the amplitude mode blue-shifts to 60 cm^{-1} in $(TPA)_yNbSe_2$ and 56 cm^{-1} in $(TBA)_xNbSe_2$, reflecting enhanced electron–phonon coupling[19]. In particular, the amplitude mode in $(TBA)_xNbSe_2$ can survive to higher temperatures than in $(TPA)_yNbSe_2$.

To quantitatively extract T_{CDW}, the spectra were fitted using a damped harmonic oscillator model (see Supplementary Figs. 13 and 14)[39]. As shown in Fig. 3-b, the soft mode in pristine $NbSe_2$ softens from 181 to 118 cm^{-1} upon cooling to T_{CDW}, below which it stabilizes. A similar trend is observed in $(TBA)_xNbSe_2$: the soft mode frequency follows a bulk-like behavior to 130 K, at which point it abruptly changes from 164.4 to 147.5 cm^{-1}. This discontinuity is accompanied by anomalies in the A_{1g} and E^1_{2g} phonon modes (see Supplementary Figs. 15–17). Concurrently, CDW modes emerge, gain intensity, harden and sharpen below 130 K, marking the onset of CDW order. These results clearly identify $T_{CDW} \approx 130$ K in $(TBA)_xNbSe_2$, showing the highest reported T_{CDW} in intercalated $NbSe_2$ to date (see Supplementary Table 2)[30,31].

To directly visualize the CDW order in real space, we performed STM measurements on $(TBA)_xNbSe_2$. Figure 4a displays representative STM topographs together with their two-dimensional Fourier transforms. A nearly perfect hexagonal atomic lattice is resolved, along with a well-defined, long-range incommensurate (~3 × 3) CDW modulation. In contrast to metal-intercalated $NbSe_2$, where defects and disorder are often introduced[40], intercalation with TBA^+ produces no observable structural defects (see Supplementary Fig. 20) and preserves the integrity of CDW. The unit cell of the superlattice closely resembles that of pristine $NbSe_2$[4], attesting to the

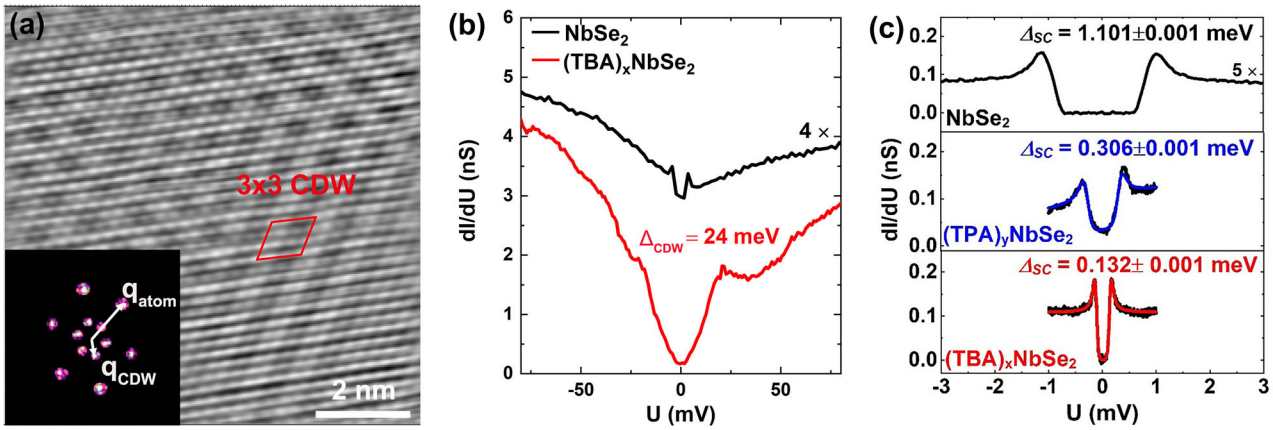

Fig. 4 | Real-space charge order and suppressed superconductivity in intercalated $NbSe_2$. **a** The STM image of the intercalated $(TBA)_xNbSe_2$. The tip was stabilized at sample bias 20 mV with tunneling current 20 pA. **b**, **c** CDW gap and superconductivity gap of $NbSe_2$ and intercalated $(TBA)_xNbSe_2$ measured at 44 mK. Measuring conditions: **a** the tip was stabled at sample bias 20 mV with tunneling current 20 pA; **b** the tip was stabled at sample bias 100 mV and tunneling current 100 pA, and the lock-in amplifier had a modulation amplitude 4 mV; **c** the tip was stabled at sample bias 5 mV and tunneling current 100 pA with modulation amplitude 50 μV for $NbSe_2$, and sample bias 1 mV and tunneling current 100 pA with modulation amplitude 15 μV for $(TPA)_yNbSe_2$ and $(TBA)_xNbSe_2$.

minimal perturbation of the host lattice by the organic cation. Disorder is an important consideration in intercalated $NbSe_2$ systems. In metal-intercalated $NbSe_2$, randomly distributed intercalants can act as strong scattering centers and disrupt the phase coherence of the CDW. In contrast, the organic cations used here primarily reside in the van der Waals gaps and act as molecular spacers. Consistent with this picture, STM measurements reveal a well-defined atomic lattice together with long-range CDW order, indicating that the in-plane CDW remains robust despite the expanded interlayer spacing. Furthermore, compared to $NbSe_2$, a wide CDW gap (Δ_{CDW}) of about 24 meV emerges near the Fermi level in $(TBA)_xNbSe_2$ (Fig. 4b). That may be caused by partial Fermi surface gapping, multiband effects, and strong coupling mechanisms[18,41]. Using the measured CDW gap ($\Delta_{CDW} \approx 24$ meV), we obtain

$$\frac{2\Delta_{CDW}}{k_B T_{CDW}} \approx 4.4,$$

exceeding the canonical weak-coupling BCS/Peierls value of 3.52[42]. This elevated ratio is a hallmark of strong electron–phonon coupling and is often associated with CDW states that deviate from a simple nesting-driven Peierls picture, consistent with prior reports on $NbSe_2$[40,43].

In addition, we investigated the effect of cation intercalation on superconductivity using STM, Raman spectroscopy, electrical transport, and magnetization. STM measurements reveal a well-defined local superconducting gap Δ_{SC} of approximately 0.31 meV for $(TPA)_yNbSe_2$ and 0.13 meV for $(TBA)_xNbSe_2$ (Fig. 4c and Supplementary Fig. 23). These values are substantially smaller than the gap of pristine $NbSe_2$ ($\Delta_{SC} \simeq 1.1$ meV)[4], demonstrating a strong reduction of the local superconducting energy scale upon intercalation.

Low-temperature transport and magnetization measurements nevertheless reveal macroscopic superconducting anomalies, with a transition below 1 K in $(TPA)_yNbSe_2$ and an onset around 3 K in $(TBA)_xNbSe_2$ (Supplementary Fig. 8). These observations show that superconductivity persists in the intercalated crystals, but also indicate that the superconducting response cannot be described by a single homogeneous weak-coupling BCS phase. In particular, combining the small local gap measured by STM in $(TBA)_xNbSe_2$ with the macroscopic transition near 3 K would yield $2\Delta_{SC}/k_B T_c \sim 1$, far below the weak-coupling BCS value. We therefore distinguish between the local superconducting gap scale probed by STM and the macroscopic superconducting transition detected by transport and magnetization.

This distinction is further supported by Raman measurements down to 2 K, which show no signature of the sharp superconductivity-induced mode observed near 19 cm^{-1} in pristine $NbSe_2$[37] (Supplementary Fig. 19). Raman measurements below 2 K would be required to directly probe the collective superconducting response of the intercalated compounds.

Discussion

The comparison between local and macroscopic probes provides important insight into the nature of superconductivity in the intercalated compounds. While STM reveals a monotonic suppression of the local superconducting gap from pristine $NbSe_2$ to $(TPA)_yNbSe_2$ and $(TBA)_xNbSe_2$, transport and magnetization detect superconducting transitions at different characteristic temperatures. This apparent discrepancy suggests that superconductivity in the intercalated crystals is spatially inhomogeneous on mesoscopic length scales. STM probes the local density of states of the cleaved, strongly intercalated $NbSe_2$ layers, where enhanced CDW order and modified carrier density suppress the superconducting gap. By contrast, transport and magnetization are sensitive to macroscopic superconducting connectivity and may therefore be influenced by regions with a different degree of intercalation, weaker charge transfer, residual interlayer coupling, or reduced local CDW competition. The superconducting anomalies observed in bulk-sensitive measurements should therefore be viewed as macroscopic onset temperatures, whereas the STM spectra provide the local superconducting energy scale of the intercalated surface/layer region.

This interpretation does not affect the central conclusion that molecular intercalation strongly enhances charge order and suppresses the local superconducting pairing scale. Rather, it highlights that intercalation introduces not only dimensional reduction and electron doping, but also a spatially non-uniform superconducting landscape. Such inhomogeneity is not unexpected in electrochemically intercalated layered crystals, where small variations in molecular filling, charge transfer, or local stacking can strongly affect superconductivity, even when the average structural expansion is well-defined by XRD and TEM.

The strong suppression of T_c observed in intercalated compounds may result from significant changes in carrier concentration introduced during the electrochemical process. Assuming that each intercalated TAA^+ cation donates one electron to the $NbSe_2$ layers, the nominal electron doping is $x = 0.22$ e/Nb for $(TBA)_xNbSe_2$. Using the in-plane lattice constant $a \simeq 3.44$ Å, the area of the two-dimensional hexagonal unit cell is $A = \frac{\sqrt{3}}{2}a^2 \simeq 1.03 \times 10^{-19}$ m^2. The corresponding two-dimensional carrier density induced by TBA^+ intercalation is therefore

$$n_{2D} = \frac{0.22}{A} \simeq 2.1 \times 10^{18}\ m^{-2} \simeq 2.1 \times 10^{14}\ cm^{-2},$$

corresponding to ~10% of the intrinsic carrier density of pristine $NbSe_2$[44]. This is consistent with several independent spectroscopic signatures, including the shift of the density-of-states peaks toward negative bias in STM measurements and the redshift of the Nb 3*d* and Se 3*d* core levels (see Supplementary Figs. 7 and 22), both of which indicate electron injection into the $NbSe_2$ layers.

Interestingly, larger electron doping achieved in $NbSe_2$ bilayers through misfit phases has recently been shown to suppress the CDW instability[17]. The contrast with our observations raises the question of whether the distinct behavior originates from the different doping amplitudes or instead reflects qualitatively different responses in monolayers and bilayers. Addressing these possibilities will be an important direction for future study.

Further insight into the superconducting state is provided by the tunneling spectra, which display pronounced dip-hump anomalies at both positive and negative bias beyond the superconducting gap (see Supplementary Fig. 23). These features appear at an energy scale compatible with interband Josephson coupling and closely resemble the signatures recently associated with Leggett collective modes in single-layer $NbSe_2$[45,46]. While a definitive identification will require momentum-resolved probes and theoretical modeling, the similarity in phenomenology lends support to this interpretation. More broadly, these results underscore the potential of intercalated bulk crystals as a platform for exploring collective excitations in multiband superconductors.

Conclusion

In summary, we have shown that electrochemical intercalation of TPA^+ and TBA^+ ions into bulk $NbSe_2$ produces a substantial expansion of the interlayer spacing and an effective electronic decoupling of the constituent layers. The interlayer distance increases from 0.62 nm in pristine $NbSe_2$ to 1.22 nm in $(TPA)_yNbSe_2$ and 1.52 nm in $(TBA)_xNbSe_2$, strongly reducing the electronic coupling between adjacent layers. This interlayer decoupling is accompanied by a pronounced enhancement of the CDW transition temperature, reaching $T_{CDW} \simeq 130$ K, together with a strong suppression of superconductivity. The resulting phase diagram closely mirrors that of exfoliated monolayers[30,47], demonstrating that molecular intercalation provides a robust and scalable route for accessing monolayer-like electronic ground states in macroscopic bulk crystals.

The concurrent enhancement of CDW order and suppression of superconductivity highlight the intrinsic competition between these two collective phenomena in $NbSe_2$. We attribute the enhanced T_{CDW} primarily to the interlayer decoupling induced by molecular intercalation, which drives the system toward the two-dimensional limit where CDW order is known to be strongly stabilized. At the same time, charge transfer from the intercalated organic cations may provide an additional tuning parameter by modifying the electronic structure, screening, and electron–phonon coupling. The quantitative carrier-density analysis, supported by XPS and STM measurements, therefore suggests that electron injection may contribute to the quantitative value of T_{CDW} and to the suppression of superconductivity, although it is not considered the primary origin of the CDW enhancement. These results establish molecular intercalation as an effective strategy for tuning the dimensionality and carrier density of layered quantum materials, thereby controlling the balance between competing electronic ground states.

Finally, the observation of dip-hump anomalies consistent with Leggett-mode-like collective excitations reveals new opportunities to investigate multiband dynamics and superconducting collective modes in the two-dimensional limit. Overall, molecular intercalation establishes a powerful platform for engineering dimensionality, carrier concentration, and competing orders in layered quantum materials, offering a promising pathway toward unraveling the microscopic mechanisms that govern unconventional charge-ordered superconductors.

Methods

Synthesis of $NbSe_2$ single crystal

$NbSe_2$ Single crystals were grown by chemical vapor transport (CVT) using iodine (99.8%, Riedel de Haën) as the transport agent. A mixture consisting of 2 g prereacted $NbSe_2$, 120 mg of iodine, and an additional 11.5 mg of selenium (99.9%, Roth) was sealed under vacuum in a fused silicon ampoule. The ampoule was then placed in a two-zone furnace, with the source and sink temperatures maintained at 810 °C and 750 °C, respectively, to facilitate directed transport. After 12 days of growth under these conditions, large plate-shaped $NbSe_2$ crystals were obtained at the cooler end of the ampoule. Single crystals were achieved by washing with ethanol to remove iodine remains (see Supplementary Fig. 1).

Intercalation of $(TAA)_x$ molecules

The intercalated $NbSe_2$ crystals were synthesized via an electrochemical intercalation process using a two-electrode system[48,49] (see Supplementary Fig. 2), where the $NbSe_2$ crystal acted as the cathode and a platinum foil was used as anode. The cathode and anode were placed in parallel with a constant distance of 1.0 cm. Tetraalkylammonium bromide (referred to hereafter as TAA^+, alkyl = propyl, butyl) in anhydrous dimethylformamide (DMF, 0.01 M, 5 mL) was chosen as electrolyte. Because tetraalkylammonium ions have an appropriate molecular size to enter the van der Waals gap, sufficient electrochemical stability over the relevant potential window, and good solubility in organic solvents. In addition, their similar chemical nature, but different alkyl-chain length and molecular size, can tune the interlayer spacing and charge transfer to affect the CDW and superconducting states of $NbSe_2$. With a low current (20–80 μA), organic cations such as TPA^+ and TBA^+ are capable of intercalating in van der Waals gaps of the $NbSe_2$ crystal (see Supplementary Fig. 2). By varying in size, the intercalated cations enable control over interlayer spacing and doping levels, making them a valuable tool to tune the electronic properties of $NbSe_2$. The associated electrochemical reactions are outlined in the following equations:

$$\text{Anode: } x\text{Br}^- - xe^- \rightarrow \frac{x}{2}\text{Br}_2$$

$$\text{Cathode: } \text{NbSe}_2 + xe^- + x\text{TAA}^+ \rightarrow (\text{TAA})_x\text{NbSe}_2$$

Electrochemical characterization of the intercalation was performed (Supplementary Fig. 4) and the compositions of the intercalated crystals were determined to be $(TPA)_{0.13}NbSe_2$ and $(TBA)_{0.22}NbSe_2$ based on the number of transferred electrons and energy-dispersive X-ray spectroscopy (see Supplementary Note 3, Supplementary Table 1 and Supplementary Figs. 5 and 2). We could further check that the intercalated $NbSe_2$ samples remain stable for at least two months (see Supplementary Fig. 18), in contrast to the monolayer counterpart, which degrades within only a few hours[50].

Low-temperature Raman spectroscopy

Polarized Raman scattering was performed using a Horiba Jobin-Yvon LabRAM HR Evolution spectrometer equipped with a liquid-nitrogen-cooled CCD detector for measurements from 10 to 290 K. A He–Ne laser (λ = 632.8 nm) with power kept below 1 mW was focused on the sample through a 50 × objective, producing a spot size of ~5 μm. To suppress elastically scattered light, the detection path included one notch filter and two Bragg filters. Spectra were acquired using 1800 mm^{-1} and 600 mm^{-1} gratings, corresponding to spectral resolutions of 0.6 cm^{-1} and 1.6 cm^{-1}, respectively. This set-up was also used to perform Raman mapping of the intercalated samples and confirm the homogeneity of the intercalation (Supplementary Fig. 11). Superconductivity mode was investigated using a Trivista triple-grating Raman spectrometer with an incident laser line at 532 nm. Measurements were taken at 2 K with a ^{4}He closed-cycle cryostat and with low power (0.05 mW) to reduce laser heating effect. All spectra were corrected for the Bose thermal population factor.

To probe excitations of different symmetries, we employed two polarization configurations: parallel (*aa*) and perpendicular (*ab*), in which the incident light polarization lies along the crystallographic *a* axis and is either parallel or perpendicular to the polarization of the scattered light, respectively. According to Raman selection rules[51], these geometries allow

access to the A_{1g}+E_{2g} and E_{2g} symmetry channels, respectively, in the hexagonal phase (point group D^1_{6h}).

Scanning tunneling microscopy

STM measurements were performed in a home-built ultra-high vacuum chamber housing a slider-type STM at milli-Kelvin temperatures[52]. The base pressure during the experiments was 10^{-10} mbar. The intercalated $NbSe_2$ was cleaved under ultra-high vacuum with Kapton tape at room temperature and then immediately transferred to STM. All STM images were recorded in constant current mode. The W tip was initially prepared by flashing in the preparation chamber and was controlled in STM by dipping it into an Au(111) substrate, as well as by voltage pulsing on $NbSe_2$. A lock-in amplifier was used for spectroscopy. The spatial uniformity of the superconducting gap was checked by acquiring tunneling spectra at several different positions on the cleaved surface of $(TBA)_xNbSe_2$ (Supplementary Fig. 21).

Data availability

The data supporting the findings of this study are available from the corresponding author upon request.

Received: 5 January 2026; Accepted: 30 June 2026;
Published online: 14 July 2026

References

1. Manzeli, S., Ovchinnikov, D., Pasquier, D., Yazyev, O. & Kis, A. 2D transition metal dichalcogenides. *Nat. Rev. Mater.***2**, 17033 (2017).
2. Wang, Q., Kalantar-Zadeh, K., Kis, A., Coleman, J. & Strano, M. Electronics and optoelectronics of two-dimensional transition metal dichalcogenides. *Nat. Nanotechnol.***7**, 699 (2012).
3. Leroux, M. et al. Strong anharmonicity induces quantum melting of charge density wave in 2H-$NbSe_2$ under pressure. *Phys. Rev. B***92**, 140303 (2015).
4. Sanna, A. et al. Real-space anisotropy of the superconducting gap in the charge-density wave material 2H-$NbSe_2$. *NPJ Quantum Mater.***7**, 6 (2022).
5. Cho, K. et al. Using controlled disorder to probe the interplay between charge order and superconductivity in $NbSe_2$. *Nat. Commun.***9**, 2796 (2018).
6. Majumdar, A. et al. Interplay of charge density wave and multiband superconductivity in layered quasi-two-dimensional materials: the case of 2H-NbS_2 and 2H-$NbSe_2$. *Phys. Rev. Mater.***4**, 084005 (2020).
7. Moncton, D. E., Axe, J. D. & DiSalvo, F. J. Study of superlattice formation in 2H-$NbSe_2$ and 2*H*-$TaSe_2$ by neutron scattering. *Phys. Rev. Lett.* **34**, 734–737 (1975).
8. Weber, F. et al. Extended phonon collapse and the origin of the charge-density wave in 2H-$NbSe_2$. *Phys. Rev. Lett.***107**, 107403 (2011).
9. Johannes, M. D., Mazin, I. I. & Howells, C. A. Fermi-surface nesting and the origin of the charge-density wave in $NbSe_2$. *Phys. Rev. B***73**, 205102 (2006).
10. Valla, T. et al. Quasiparticle spectra, charge-density waves, superconductivity, and electron-phonon coupling in 2H-$NbSe_2$. *Phys. Rev. Lett.***92**, 086401 (2004).
11. Berthier, C., Molinie, P. & Jerome, D. Evidence for a connection between charge density waves and the pressure enhancement of superconductivity in 2H-$NbSe_2$. *Solid State Commun.***18**, 1393 (1976).
12. Suderow, H., Tissen, V. G., Brison, J. P., Martínez, J. L. & Vieira, S. Pressure induced effects on the Fermi surface of superconducting 2H-$NbSe_2$. *Phys. Rev. Lett.***95**, 117006 (2005).
13. Feng, Y. et al. Order parameter fluctuations at a buried quantum critical point. *Proc. Natl. Acad. Sci. USA***109**, 7224 (2012).
14. Gao, S. et al. Atomic-scale strain manipulation of a charge density wave. *Proc. Natl. Acad. Sci. USA***115**, 6986 (2018).
15. Rouxel, J., Meerschaut, A. & Wiegers, G. Chalcogenide misfit layer compounds. *J. Alloy. Compd.***229**, 144 (1995).
16. Leriche, R. T. et al. Misfit layer compounds: a platform for heavily doped 2D transition metal dichalcogenides. *Adv. Funct. Mater.***2021**, 2007706 (2020).
17. Zullo, L. et al. Charge density wave collapse of $NbSe_2$ in the $(LaSe)_{1.14}NbSe_2$ misfit layer compound. *Phys. Rev. B***110**, 075430 (2024).
18. Ugeda, M. et al. Characterization of collective ground states in single-layer $NbSe_2$. *Nat. Phys.***12**, 92 (2016).
19. Xi, X. et al. Strongly enhanced charge-density-wave order in monolayer $NbSe_2$. *Nat. Nanotechnol.***10**, 765 (2015).
20. Baidya, P. et al. Transition from three- to two-dimensional Ising superconductivity in few-layer $NbSe_2$ by proximity effect from van der Waals heterostacking. *Phys. Rev. B***104**, 174510 (2021).
21. Cao, Y. et al. Quality heterostructures from two-dimensional crystals unstable in air by their assembly in inert atmosphere. *Nano Lett.***15**, 4914 (2015).
22. Xi, X. et al. Ising pairing in superconducting $NbSe_2$ atomic layers. *Nat. Phys.***12**, 139 (2016).
23. Nakata, Y. et al. Anisotropic band splitting in monolayer $NbSe_2$: implications for superconductivity and charge density wave. *NPJ 2D Mater. Appl.***2**, 12 (2018).
24. Zheng, F. & Feng, J. Electron-phonon coupling and the coexistence of superconductivity and charge-density wave in monolayer $NbSe_2$. *Phys. Rev. B***99**, 161119 (2019).
25. Wickramaratne, D., Khmelevskyi, S., Agterberg, D. F. & Mazin, I. I. Ising superconductivity and magnetism in $NbSe_2$. *Phys. Rev. X***10**, 041003 (2020).
26. Moulding, O., Osmond, I., Flicker, F., Muramatsu, T. & Friedemann, S. Absence of superconducting dome at the charge-density-wave quantum phase transition in 2H-$NbSe_2$. *Phys. Rev. Res.***2**, 043392 (2020).
27. Wan, Z. et al. Unconventional superconductivity in chiral molecule TaS_2 hybrid superlattices. *Nature***632**, 69 (2024).
28. Dresselhaus, M. & Dresselhaus, G. Intercalation compounds of graphite. *Adv. Phys.***30**, 139 (1981).
29. Luo, H. et al. S-shaped suppression of the superconducting transition temperature in Cu-intercalated NbSe2. *Chem. Mater.***29**, 3704 (2017).
30. Zhang, H. et al. Tailored Ising superconductivity in intercalated bulk $NbSe_2$. *Nat. Phys.***18**, 1425 (2022).
31. Yu, L. et al. Intercalation-induced monolayer behavior in bulk $NbSe_2$. *ACS Appl. Mater. Interfaces***16**, 59049 (2024).
32. Grasset, R. et al. Higgs-mode radiance and charge-density-wave order in 2H-$NbSe_2$. *Phys. Rev. B***97**, 094502 (2018).
33. Tan, P. et al. The shear mode of multilayer graphene. *Nat. Mater.***11**, 294 (2012).
34. Roth, W. et al. Exfoliated ferrierite-related unilamellar nanosheets in solution and their use for preparation of mixed zeolite hierarchical structures. *J. Am. Chem. Soc.***1643**, 11052 (2012).
35. Sen, K. et al. Strange semimetal dynamics in $SrIrO_3$. *Nat. Commun.***11**, 4270 (2020).
36. Tsang, J. C., Smith, J. E. & Shafer, M. W. Raman spectroscopy of soft modes at the charge-density-wave phase transition in 2H-$NbSe_2$. *Phys. Rev. Lett.***37**, 1407 (1976).
37. Sooryakumar, R. & Klein, M. V. Raman scattering by superconducting-gap excitations and their coupling to charge-density waves. *Phys. Rev. Lett.***45**, 660 (1980).
38. Méasson, M. A. et al. Amplitude Higgs mode in the 2H-$NbSe_2$ superconductor. *Phys. Rev. B***89**, 060503 (2014).
39. Cao, Z. et al. Pressure effect of the charge density wave transition on Raman spectra and transport properties of 2H-$NbSe_2$. *Phys. Rev. B***107**, 245125 (2023).
40. Chatterjee, U. et al. Emergence of coherence in the charge-density wave state of 2H-$NbSe_2$. *Nat. Commun.***6**, 6 (2015).

41. Wang, C., Giambattista, B., Slough, C. G., Coleman, R. V. & Subramanian, M. A. Energy gaps measured by scanning tunneling microscopy. *Phys. Rev. B***42**, 8890 (1990).
42. Bardeen, J., Cooper, L. N. & Schrieffer, J. R. Theory of superconductivity. *Phys. Rev.***108**, 1175 (1957).
43. Borisenko, S. V. et al. Two energy gaps and Fermi-surface "Arcs" in $NbSe_2$. *Phys. Rev. Lett.***102**, 166402 (2009).
44. Xi, X., Berger, H., Forró, L., Shan, J. & Mak, K. F. Gate tuning of electronic phase transitions in two-dimensional $NbSe_2$. *Phys. Rev. Lett.***117**, 106801 (2016).
45. Leggett, A. J. Number-phase fluctuations in two-band superconductors. *Prog. Theor. Phys.***36**, 901 (1966).
46. Wan, W. et al. Observation of superconducting collective modes from competing pairing instabilities in single-layer $NbSe_2$. *Adv. Mater.***34**, 2206078 (2022).
47. Nakata, Y. et al. Robust charge-density wave strengthened by electron correlations in monolayer 1T-$TaSe_2$ and 1T-$NbSe_2$. *Nat. Commun.***12**, 5873 (2021).
48. Shi, H. et al. High-throughput synthesis of solution-processable van der Waals heterostructures through electrochemistry. *Angew. Chem. Int. Ed.***62**, e202303929 (2023).
49. Shi, H. et al. Ultrafast electrochemical synthesis of defect-free In_2Se_3 flakes for large-area optoelectronics. *Adv. Mater.***32**, 1907244 (2020).
50. Wang, H. et al. High-quality monolayer superconductor $NbSe_2$ grown by chemical vapour deposition. *Nat. Commun.***8**, 394 (2017).
51. Hayes, W. & Loudon, R. *Scattering of Light by Crystals* (John Wiley and Sons, 1978).
52. Balashov, T., Meyer, M. & Wulfhekel, W. A compact ultrahigh vacuum scanning tunneling microscope with dilution refrigeration. *Rev. Sci. Instrum.***89**, 113707 (2018).

Acknowledgements

We thank S. Souliou, M. Frachet, and C. Singh for fruitful discussion and we are grateful to the Karlsruhe Nano-Micro Facility (KNMFi) for technical support. We acknowledge the funding by the European Research Council (ERC) under the European Union's Horizon 2020 research and innovation programme (Grant Agreement No. 865826), the Deutsche Forschungsgemeinschaft (DFG, German Research Foundation), Grant No. TRR 288-422213477 (Project B03, B06, and B10), Project No. 449386310, and CRC FLAIR.

Author contributions

H.S. and M.L.T. conceived the project. H.S., F.H., P.B., A.B., M.-A.M., and M.L.T. performed the polarized Raman scattering measurements and carried out the Raman data analysis. Q.L., A.H., and W.W. conducted the STM experiments. S.K., D.W., and C.K. performed the TEM experiments. D.F., N.M., and M.M. performed the XRD measurements. K.S. and E.H. performed the transport measurements. A.-A.H. grew the single crystals. H.S. synthesized the intercalated crystals. H.S. and M.L.T. wrote the manuscript with input from all authors.

Funding

Open Access funding enabled and organized by Projekt DEAL.

Competing interests

The authors declare no competing interests.

Additional information

Supplementary information The online version contains supplementary material available at https://doi.org/10.1038/s43246-026-01270-2.

Correspondence and requests for materials should be addressed to Huanhuan Shi or Matthieu Le Tacon.

Peer review information *Communications Materials* thanks Huixia Luo, Golam Haider for their contribution to the peer review of this work.